Acta Geotechnica (2022) 17:2101–2119
https://doi.org/10.1007/s11440-021-01388-2

RESEARCH PAPER

SPH-DEM coupling method based on GPU and its application to the landslide tsunami. Part I: method and validation

Qian Zhou[1] · Wen-Jie Xu[1] · Xue-Yang Dong[1]

Received: 5 May 2021 / Accepted: 10 October 2021 / Published online: 2 November 2021

Abstract
Landslide-induced tsunami is a complex fluid–solid coupling process that plays a crucial role in the study of a disaster chain. To simulate the coupling behaviors between the fluid and solid, a graphics processing unit-based coupled smoothed particle hydrodynamics (SPH)-discrete element method (DEM) code is developed. A series of numerical tests, which are based on the laboratory test by Koshizuka et al. (Particle method for calculating splashing of incompressible viscous fluid, 1995) and Kleefsman et al. (J Comput Phys 206:363–393, 2005), are carried out to study the influence of the parameters, and to verify the accuracy of the developed SPH code. To ensure accurate results of the SPH simulation, the values for the diffusion term, particle resolution (1/25 characteristic length), and smoothing length (1.2 times of particle interval) are suggested. The ratio of the SPH particle size and the DEM particle's diameter influences the accuracy of the coupling simulation between solid particles and water. For the coupling simulation of a single particle or a loose particle assembly (not contact each other) with fluid, this ratio should be smaller than 1/20; for a dense particle assembly, a ratio of smaller than 1/6 will be good.

Keywords Dam break · Fluid–solid coupling algorithm · Graphics processing unit (GPU) · Landslide tsunami · SPH–DEM

1 Introduction

Tsunamis generated by landslides are caused by landslides near water or submarine and are one of the most important contributors to the disaster chain [10, 13, 31, 34]. They directly endanger water channels, residents and structures close to a reservoir, and often lead to huge catastrophes. The analysis of these disasters has been a pending challenge due to the complex "fluid–solid" coupling process between the landslide, and the water with a highly fragment-free surface that appears in the wave propagation. Furthermore, the fluid–solid coupling is also a common phenomenon in nature, for example, landslide tsunami, seepage process [11, 14], debris flow [21], dam break [26], and so on. In recent years, studies on fluid–solid coupling are becoming a hotspot in many fields [29, 42]. Conventional laboratory tests can provide experiences and examples for researchers, but can hardly reveal the inherent mechanism for fluid–solid coupling due to the limited technical methods, while numerical methods have gradually developed maturely to understand the comprehensive mechanism between solid and fluid.

Mesh-based numerical methods such as the finite element method (FEM) and the finite volume method (FVM) together with fluid, solid and fluid–solid interaction constitutive models have been developed to simulate the evolution of fluid in fluid–solid systems [24, 28, 46, 58] with both high efficiency and accuracy. However, the reliance on mesh makes it difficult to simulate discontinuous behaviors like a wave breaking. Conversely, particle-based methods, in which particles interact with each other under specific constitutive models, are generally less efficient. The positions of free particles are usually unpredictable which brings difficulties in programming such as interaction detection, memory management, which may lead to high computational complexity. Fortunately, with

✉ Wen-Jie Xu
wenjiexu@tsinghua.edu.cn

[1] State Key Laboratory of Hydroscience and Hydraulic Engineering, Department of Hydraulic Engineering, Tsinghua University, Beijing 100084, China

the advances in Graphics Processing Unit (GPU) and pertinent parallel algorithms, particle-based methods have gradually shown advantages in simulating complex discontinuous physical processes.

The discrete element method (DEM), firstly proposed by Cundall and Strack [6], is one of the representative particle-based methods that can simulate the discontinuous and heterogeneous behaviors of granular materials such as particle breakage [12], rock failure [30], grinding mill [16, 45] and landslide[56]. In recent years, to simulate the more complex physical process,, algorithms have been developed to couple DEM with other numerical methods like FEM [18, 44, 57], LBM [11, 27], SPH [50], where DEM is used to simulate the discontinuous solid phase. As for the fluid phase, the smoothed particle hydrodynamics (SPH), carried out by Monaghan [15], plays an important role in the analysis of flood disasters, such as dam break [7], tsunamis [47, 51, 53], seepage failure [41]. SPH also uses particles to represent the computing domain and solves the Navier–Stokes equations. In recent years, SPH is implemented in the simulation of geomaterials [60].

Generally, to decrease the size effect on the numerical results, the particle scales in both DEM and SPH are limited based on the computing models, which usually results in a large number of particles, and thus increases the burden of the computational cost. This problem is especially serious for SPH as the particles in 3D simulation interact with more than 100 surrounding particles, not to mention that the number of particles is usually quite large. Fortunately, with high-performance GPU and relative parallel algorithms, the computing efficiency is no longer a bottleneck in DEM and SPH simulations. GPU-based DEM programs [17] and SPH programs [9, 20] have been proven efficient in large-scale simulations.

With the development of numerical methods in recent years, simulations with multi-phase, multi-process, multi-scale became increasingly important. Among them is the SPH–DEM coupling algorithm which is crucial for solid–fluid coupling processes in a variety of aspects. Wu et al. [50] tested the influence of the kernel functions, smooth length, and particle resolution on SPH and verified the coupling algorithm using a dam break model with solid fracture. Tan et al. [47] simulated the surge waves triggered by rock block and granular deformable material, respectively. Sarfaraz et al. [43] and Ren et al. [40] analyzed the hydraulic stability of blocks on a slope with a wave generation method. The aforementioned works correspond well with laboratory results but are performed on 2D models.

In 3D simulations of SPH–DEM, Yi [19] and Sinnott [45] simulated solid–fluid mixture in a roller, respectively, and Shungo [38] analyzed the trickle flow in coke bed and the static holdup droplets is similar to estimation. Peng, Zhan, etc. [39, 54, 55] developed the SPH–DEM algorithms for arbitrary shaped particles and fluid. Using the laboratory test of the water-entry process of a single sphere, Xu et al. [52] verified the SPH–DEM algorithm and used it to simulate a practical landslide tsunami disaster [53]. Kermani [22] simulated the collapse of granular columns in which SPH is used to simulate the granular material. Wang et al. [48] simulated the landslide-induced tsunami in Yangtze River using a combined FDEM-SPH method. The previous studies are mainly focused on classical numerical tests or the simulation of laboratory tests and they are mostly performed on a single GPU. However, when it comes to the simulation of the practical cases, the computational scale sometimes got quite large. For instance, over 30 million SPH particles are used in the simulation of the Lijiaxia reservoir [53]. In this case, a multi-GPU-based SPH–DEM method can further increase computing efficiency and eliminate the limitation of GPU memory cost. Numerical methods provide a powerful tool to study the failure mechanisms and the dynamic process of geohazards. Before a numerical method can be considered as a useful tool for the analysis of the actual cases, it should overcome at least two verification steps [5]: first, it must be validated by a series of benchmarks based on theory solution or model tests; then, it should also be verified by practical cases on-site. In this study, to efficiently perform the large-scale fluid–solid simulations, a SPH–DEM coupling algorithm based on multi-GPU is introduced and validated by benchmarks. While in the companion paper, it will be validated by a practical case.

To validate the developed code, two dam break laboratory tests are used, and the influence of smooth length, the precision of model, and δ-SPH term are studied. Then, the water-entry of a single sphere is simulated and compared with the laboratory test to verify the accuracy of the coupling algorithm. Furthermore, to provide a foundation for generating the model in practical cases, the results of the water entry test and the simple tsunami test are discussed to determine the particle resolution required for the coupling algorithm.

2 Algorithms

2.1 Discrete element method (DEM)

In DEM, particles in the computing domain follow Newton's second law,

$$m\boldsymbol{a} = \boldsymbol{F}^{C} + \boldsymbol{F}^{E} + \boldsymbol{F}^{\mathrm{damp}} \tag{1}$$

$$I\boldsymbol{\beta} = \boldsymbol{M}^{C} + \boldsymbol{M}^{E} + \boldsymbol{M}^{\mathrm{damp}} \tag{2}$$

where, m, I, $\boldsymbol{\alpha}$, $\boldsymbol{\beta}$, $\boldsymbol{F}$,$\boldsymbol{M}$ are the mass, inertia, translational acceleration, rotational acceleration, resultant force, and resultant moment of particles, respectively. Both resultant force and moment consist of contact force/moment, external force/moment and damping, which are donated by superscript C, E, $damp$, respectively.

The contact forces between particle $\boldsymbol{A}$ and particle $\boldsymbol{B}$ are calculated based on their geometries and materials. In this study, the spherical particles and cohesive fractural material (CFM) [30] are used to simulate the solid phase (Fig. 1). When two spherical particle $\boldsymbol{A}$ and $\boldsymbol{B}$ are in contact with the penetration depth of u^n and shear increment $\Delta \boldsymbol{u}^s$, the contact force for particle $\boldsymbol{A}$ in response to particle $\boldsymbol{B}$ consists of the normal force $\boldsymbol{F}^{Cn}$ and shear force $\boldsymbol{F}^{Cs}$,

$$\boldsymbol{F}_A^C = \boldsymbol{F}^{Cn} + \boldsymbol{F}^{Cs} \tag{3}$$

$$\boldsymbol{F}^{Cn} = k_n u^n \boldsymbol{n} \tag{4}$$

$$\boldsymbol{F}^{Cs} = \left\{\boldsymbol{F}^{Cs}\right\}_{\text{update}} + k_s \Delta \boldsymbol{u}^s \tag{5}$$

where, k_n and k_s are normal and shear stiffness, respectively, both calculated from the two-spring model. The stiffnesses are found by

$$\frac{1}{k_n} = \frac{1}{E_A r_A} + \frac{1}{E_B r_B} \tag{6}$$

$$\frac{1}{k_s} = \frac{1}{E_A v_A r_A} + \frac{1}{E_B v_B r_B} \tag{7}$$

where $E_{A/B}$, $v_{A/B}$,$r_{A/B}$ are Young modulus, shear to normal stiffness ratio, and radius of $\boldsymbol{A}$ and $\boldsymbol{B}$, respectively.

In this study, triangular meshes are used for the boundaries of the model (such as the slope boundary and the terrain). A sphere–triangle interaction algorithm is introduced [59], and for the contacts between spheres $\boldsymbol{A}$ and triangle boundary $\boldsymbol{B}$, r_B in Eqs. 6 and 7 is replaced with the radius of $\mathbf{A}$.

The contact moment for particle $\boldsymbol{A}$ can be decomposed to moment induced by shear force (T) and relative rotation,

$$\boldsymbol{M} = \boldsymbol{T} + \boldsymbol{M}_\text{r} + \boldsymbol{M}_\text{t} \tag{8}$$

where $\boldsymbol{M}_{\text{r/t}}$ ($\boldsymbol{M}_\text{r}$ and $\boldsymbol{M}_\text{t}$) is the rolling and twisting moment, controlled by rolling and twisting stiffness ($K_{\text{r/t}}$), relative rotation angle ($\emptyset_{r/t}$) and maximum moment value ($M_{\text{r/t}}^{\max}$). The moments are found by

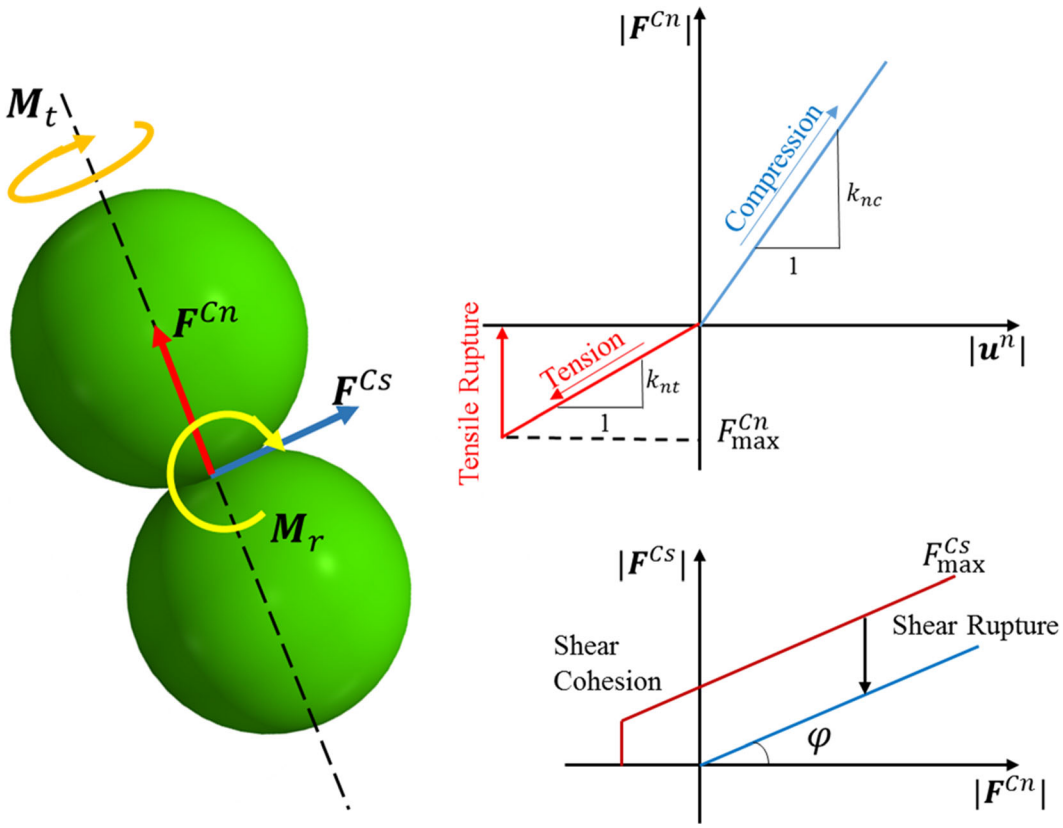

Fig. 1 DEM contact model used in this study

$$\boldsymbol{M}_{\mathrm{r/t}} = \begin{cases} K_{\mathrm{r/t}}\emptyset_{r/t} & \left|K_{\mathrm{r/t}}\emptyset_{r/t}\right| < M_{\mathrm{r/t}}^{\max} \\ M_{\mathrm{r/t}}^{\max}\dfrac{\emptyset_{r/t}}{\left|\emptyset_{r/t}\right|} & \left|K_{\mathrm{r/t}}\emptyset_{r/t}\right| > M_{\mathrm{r/t}}^{\max} \end{cases} \tag{9}$$

$$K_{r/t} = k_{r/t}(r')^2 k_s \,; r' = \min(r_A, r_B) \tag{10}$$

$$M_{r/t}^{\max} = k_{r/t}^{\max}\left|F^{Cn}\right| r'; r' = \min(r_A, r_B) \tag{11}$$

where $k_{\mathrm{r/t}}^{\max}$ is the rolling and twisting strength coefficient, $k_{\mathrm{r/t}}$ is the rolling and twisting stiffness coefficient.

In CFM, to simulate the failure process of granular materials with a certain strength, cohesion between particles are considered with the maximum normal tensile ($F_{\max}^{Cn}$) and shear tensile ($F_{\max}^{Cs}$),

$$F_{\max}^{Cn} = C_n r'^2; r' = \min(r_A, r_B) \tag{12}$$

$$F_{\max}^{Cs} = F^{Cn}\tan\varphi + C_{\mathrm{s}} r'^2; r' = \min(r_A, r_B) \tag{13}$$

where C_{n} and C_{s} are normal and shear cohesion coefficient, respectively, φ is the frictional angle based on Mohr–Coulomb law. The contact is fractured when the normal tensile force or shear force exceeds the limited maximum value.

2.2 Smoothed particle hydrodynamics (SPH)

In SPH, each particle carries the physical properties (such as the position, velocity, density and pressure) of a certain amount of fluid around it, which forms the total fluid domain in combination. The integral approximation within the region of compact support near a specific point is used to estimate its values using the kernel function (W),

$$f(\boldsymbol{r}) = \int f(\boldsymbol{r}')W(r - \boldsymbol{r}', h)\mathrm{d}\boldsymbol{r}' \tag{14}$$

where h is the smoothing length which defines the size of the region of compact support. The discrete form of the integral formula (14) in SPH together with the gradient form can be written as,

$$f(\boldsymbol{r}_i) \approx \sum_j f(\boldsymbol{r}_j)W(\boldsymbol{r}_i - \boldsymbol{r}_j, h)\frac{m_j}{\rho_j} \tag{15}$$

$$\nabla f(\boldsymbol{r}_i) \approx -\sum_j f(\boldsymbol{r}_j)\nabla W(\boldsymbol{r}_i - \boldsymbol{r}_j, h)\frac{m_j}{\rho_j} \tag{16}$$

where, subscript i and j donates the SPH particles, m_j and ρ_j is the mass and density of particle j, respectively. The smoothing kernel function (W) is crucial to the performance of SPH simulation as it influences precision and numerical stability. In this study, the quintic polynomial by Wendland [49] is used,

$$W(\boldsymbol{r}_i - \boldsymbol{r}_j, h) = \alpha_D \begin{cases} \left(1 - \dfrac{q}{2}\right)^4(1 + 2q) & 0 \le q < 2 \\ 0 & 2 \le q \end{cases} \tag{17}$$

where $q = |\boldsymbol{r}_i - \boldsymbol{r}_j|/h$, $\alpha_D = 21/(16\pi)$ in 3D condition. The Wendland kernel function is illustrated in Fig. 2.

During the simulation loop, the weakly compressible equation of state is firstly applied to determine the pressure based on particle density [37],

$$p_i = \frac{c_0^2\rho_0}{\gamma}\left(\left(\frac{\rho_i}{\rho_0}\right)^{\gamma} - 1\right) \tag{18}$$

where p_i and ρ_i are pressure and density of particle i, respectively, γ = 7.0 is the adiabatic exponent,ρ_0 = 1000 is the reference density, $c_0 = \eta\sqrt{gh_{\max}}$, η is the sound coefficient and $h_{\max}$ is the maximum water depth. The fluid dynamic is controlled by the continuity equation and momentum equation. These two equations in SPH form can be written as,

$$\frac{\mathrm{d}\rho_i}{\mathrm{d}t} = -\sum_j m_j(\boldsymbol{v}_i - \boldsymbol{v}_j + \Delta_{ij})\nabla W(\boldsymbol{r}_i - \boldsymbol{r}_j, h) \tag{19}$$

$$\frac{\mathrm{d}v_i}{\mathrm{d}t} = \sum_j m_j\left(\frac{p_i + p_j}{\rho_i\rho_j} + \Pi_{ij}\right)\nabla W(\boldsymbol{r}_i - \boldsymbol{r}_j, h) + \boldsymbol{g} \tag{20}$$

where, $\boldsymbol{v}_i$ is the velocity of particle i, Π_{ij} is artificial viscosity [36],

$$\Pi_{ij} = -\alpha\frac{hc_0}{\rho_i + \rho_j}\min\left[0, \frac{(v_i - v_j)\cdot(\boldsymbol{r}_i - \boldsymbol{r}_j)}{|r_i - r_j|^2 + 0.01h^2}\right] \tag{21}$$

where α is the artificial viscosity coefficient. The use of artificial viscosity term has proven effective to diffuse the sharp variations in the flow for practical problems. However, standard artificial viscosity is not sufficient to prevent large oscillations on the pressure field for hydrodynamic problems. So, the artificial density diffusion term called δ-SPH [3, 33, 35] is added to the continuity equation,

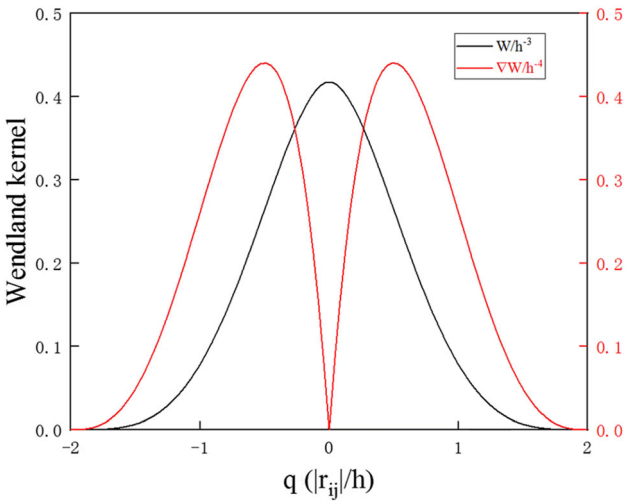

Fig. 2 Wendland kernel function used in this study

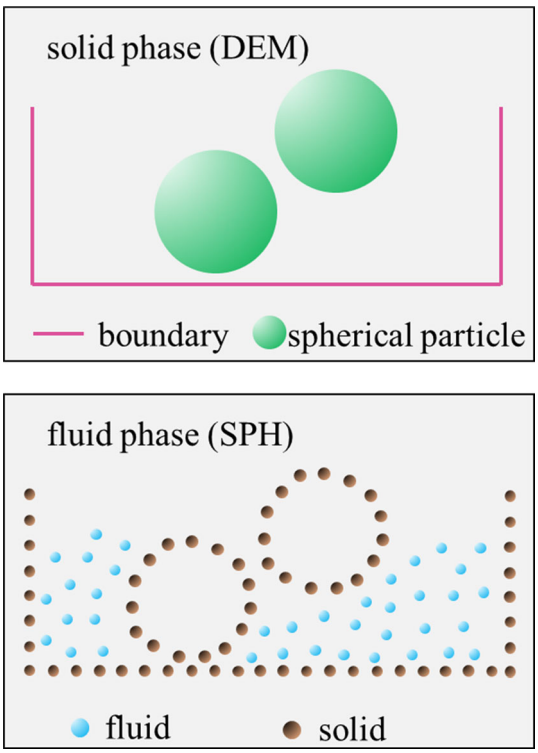

Fig. 3 Discretization of DEM model in SPH–DEM coupling algorithm

$$\Delta_{ij} = -\delta \frac{4hc_0}{\rho_i + \rho_j} \frac{(\rho_i - \rho_j)(\boldsymbol{r}_i - \boldsymbol{r}_j)}{|\boldsymbol{r}_i - \boldsymbol{r}_j|^2 + 0.01h^2} \tag{22}$$

where δ is the artificial density diffusion coefficient.

It's worth noting that, for a specific SPH particle, the surrounding particles between 0.5 h and 1.0 (Fig. 2) have a severe impact on the calculation of the particle dynamics, thus influencing the performance of the whole simulation.

2.3 SPH–DEM coupling algorithm

Ghost particles are widely used to represent the boundary of solid [1] in SPH. In this study, the surfaces of DEM particles and general boundaries are discretized to several layers of particles, which are called "solid particles" (Fig. 3). For solid particles, only fluid particles contribute to their density and velocity increment in Eqs. (19) and (20), while fluid particles interact with both solid and fluid particles.

The summation of particle acceleration obtained by momentum equation will be added to the external force/moment of DEM particles,

$$\boldsymbol{F}_k^E = \sum_b m_b \left(\frac{\mathrm{d}v_b}{\mathrm{d}t} - \boldsymbol{g} \right) + m_k \boldsymbol{g} \tag{23}$$

$$\boldsymbol{M}_k^E = \sum_b m_b \left(\frac{\mathrm{d}v_b}{\mathrm{d}t} - \boldsymbol{g} \right) \times (\boldsymbol{r}_b - \boldsymbol{r}_k) \tag{24}$$

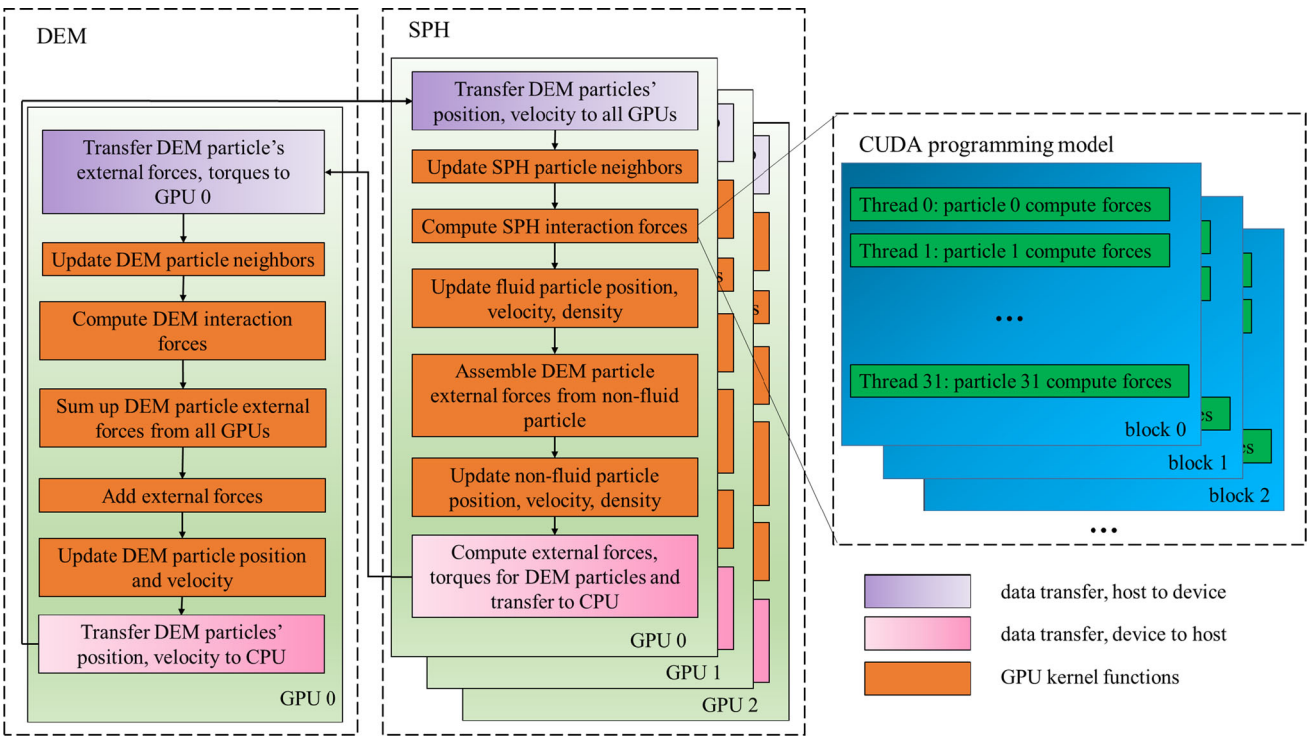

Fig. 4 Flowchart of the SPH–DEM coupling method based on multi-GPU

where b donates the SPH particles on the surface of DEM particle k, r_k is the center of particle k.

The position and velocity of SPH particles on DEM particles are updated based on their motion information,

$$\frac{d\boldsymbol{r}_b}{dt} = \boldsymbol{v}_b \tag{25}$$

$$\boldsymbol{v}_b = \boldsymbol{v}_k + \omega_k \times (\boldsymbol{r}_{b0} - \boldsymbol{r}_k) \tag{26}$$

where ω_k is the angular velocity of particle k, r_{b0} is the position of particle b before the update.

2.4 Neighbor search method

Particles in both DEM and SPH interact with surrounding particles and finding the particles (broad phase collision detection) may be time-consuming without an optimized algorithm. In general, there are many parallel searching algorithms available for broad phase detection including cell-based methods [2, 59] and hierarchical-based methods [32]. The uniform grid method, one of the widely used searching algorithms which discretize the computing domain into uniform cells, can be simply implemented in parallel programming with high efficiency. In this study, uniform grid methods are used to detect interactions for DEM and SPH, respectively.

2.5 GPU-based SPH–DEM framework

Compute Unified Device Architecture (CUDA) is a general-purpose parallel computing platform and programming model designed for the NVIDIA GPU accelerator. In CUDA, the GPU together with its memory is designed as a separate "device" in contrast to CPU and its memory on "host." Tasks are delivered to the streaming processors (SP) and streaming multiprocessors (SM) on GPU by the abstracted concepts "threads," "blocks," and "grids," which simplifies the parallel programming (Fig. 4).

Based on the aforementioned algorithm, a GPU-based coupling simulator named as CoSim is developed. Figure 4 shows the flowchart of the SPH–DEM coupling algorithm that runs on multi-GPU. In the SPH–DEM coupling

Table 1 Parameters of classical dambreak test cases T1-T5

Test case	α	δ	h/dp
T1	0.0	0.0	1.2
T2	0.01	0.1	1.2
T3	0.01	0.1	1.0
T4	0.01	0.1	1.5
T5	0.01	0.1	2.0

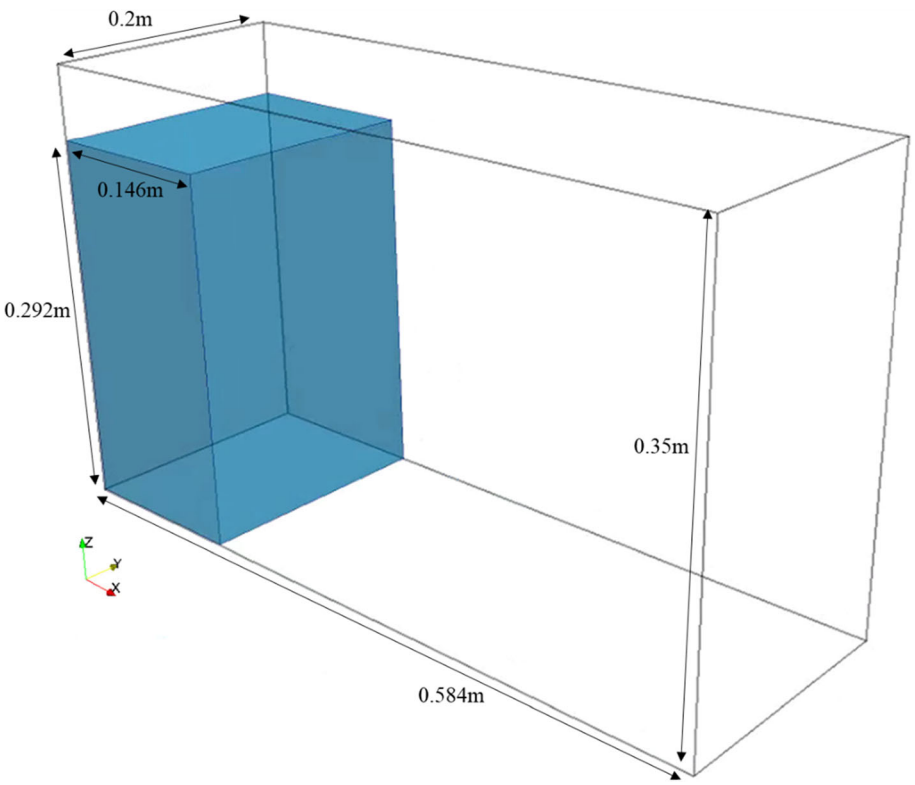

Fig. 5 Numerical model of the dambreak test I

models, the size of SPH particles is required to be several times smaller than DEM particles, so the computing cost for DEM is much smaller than SPH. As a consequence, the computation of DEM is restricted on the first GPU while the SPH particles are evenly distributed to the available GPUs. In the simulation, the SPH computation domain is evenly divided and each GPU handle a subdomain. There are overlap regions between subdomains and the information of SPH particles in the overlap regions are transferred between devices.

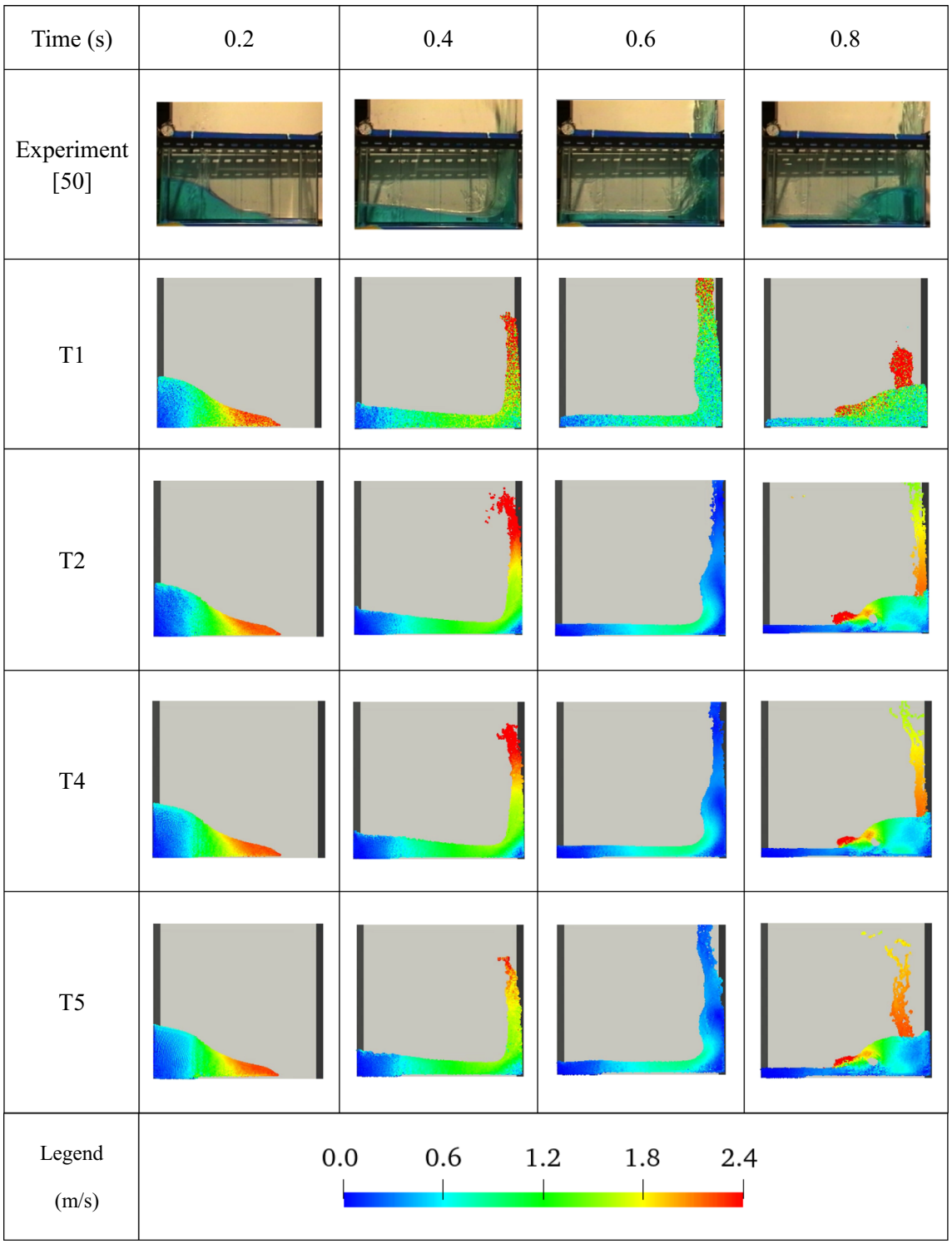

Fig. 6 The evolution of flow field from experiment and numerical results T1, T2, T4, T5 at different times

During the main loop, the basic information of all SPH particles including position, velocity, density, and pressure is firstly synchronized to each GPU. The SPH particles are sorted based on their positions and then used for the calculation of density increment and acceleration on different GPUs. The position, velocity, and density of fluid particles are updated based on the Verlet scheme while the resultant forces on DEM spheres are collected from solid SPH particles and transferred to the device of DEM. After the DEM part is finished, the positions, velocities and angular velocities of DEM spheres are transferred to other GPUs and the basic information of solid SPH particles can be updated. Finally, the pressures of all SPH particles are computed by the state equation.

3 Validation of SPH algorithm

3.1 Dambreak test I

In this section, a dambreak laboratory test by Koshizuka [25] is used to study the influence of artificial viscosity term (α), artificial density diffusion term (δ) and the smoothing length (h) on the numerical results. As shown in Fig. 5, a tank of 0.584 m × 0.2 m × 0.35 m has a water column of 0.146 m × 0.2 m × 0.292 m blocked on the left side. Five parallel numerical tests (T1-T5) with particle interval dp = 4.17 mm are performed and the parameters are shown in Table 1.

The computation of T3 doesn't converge during simulation which indicates the smoothing length should be larger than 1.0dp. The velocity distributions of the other four tests and experimental results at different times are shown in Fig. 6. It can be seen from T1&T2 (Fig. 6) that

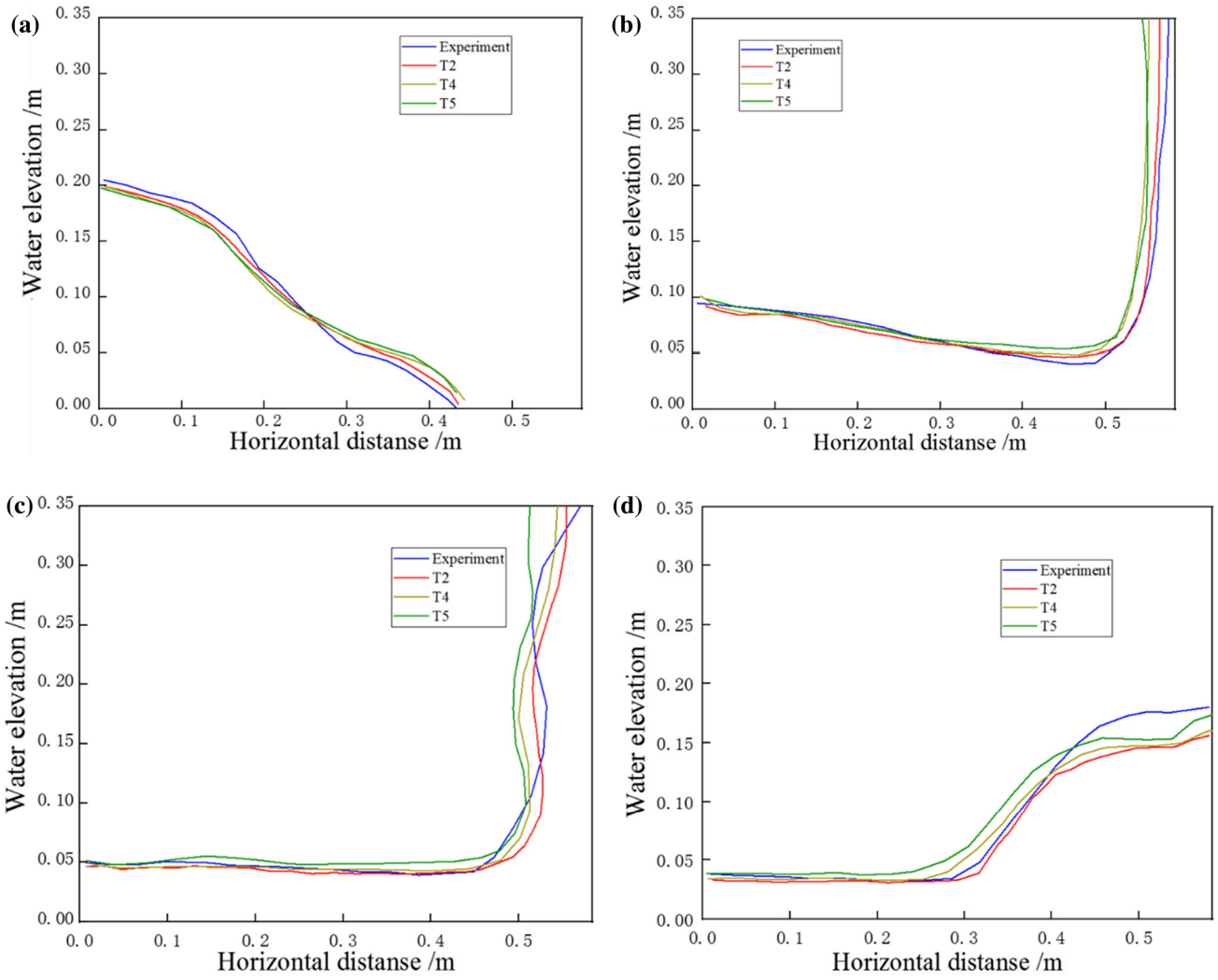

Fig. 7 The water surface of the numerical simulation and experiment: **a** 0.2 s; **b** 0.4 s; **c** 0.6 s; **d** 0.8 s

the diffusion terms effectively reduce the numerical noise of the velocity field. So, they are widely used in SPH and have been proven effective in 2D cases [33, 47]. From the results, the diffusion terms $\alpha = 0.01, \delta = 0.1$ are also suitable for 3D simulations and will be applied in the following simulations.

Comparing the experimental results and the three numerical results, it can be seen that the results obtained by simulation are in well agreement with the laboratory test (Fig. 6). The collapsing water flows quickly toward the right boundary with the maximum speed of 2.4 m/s in the front (Fig. 6, 0.2 s), impact and runs upwards along the right boundary (Fig. 6, 0.4 and 0.6 s). The returning wave gradually forms at 0.6 s and split the vertical water into two parts (Fig. 6, 0.8 s): the bottom main wave that returns fast to the left and the top splashes that fall slowly.

The water surfaces of the three numerical results correspond well with that of the experiment at different times. Taking T2 as an example, Fig. 7 shows the water surface of the numerical results and experimental results at different times. The SPH algorithm can accurately simulate the fluid phase when the smoothing length ranges from 1.2dp to 2.0dp.

It's worth noting that the flow pattern of the three tests are approximately identical and matches well with the experiment (Fig. 6) except for two differences: (a) there is a gap between the bottom boundary and the fluid in numerical tests; (b) the splash in the experiment flows down along the right boundary while the splash is "pushed back" in numerical simulation. As is shown in Eqs. (18–20), when the fluid flows across the bottom boundary at an initial stage, the density of the bottom fluid particles and solid boundary will increase (Eq. 19), thereby causing a high-pressure field near the bottom boundary (Eq. 18). Comparing the three tests, due to the numerical characters of the kernel function (Fig. 2), the "gap effect" will decrease with the decrease of the smoothing length. When the water runs upwards along the right wall (Fig. 6, 0.6 s and 0.8 s), the same numerical phenomenon occurred and it can be seen that the larger the smoothing length, the more the splash was pushed back from the wall.

So, the value of the smoothing length h can greatly influence the interaction between the fluid and the solid boundaries. To decrease the boundary effect caused by ghost particles, a smaller smoothing length is suggested to be used. According to the previous analysis, h = 1.2dp will be used in the following simulation.

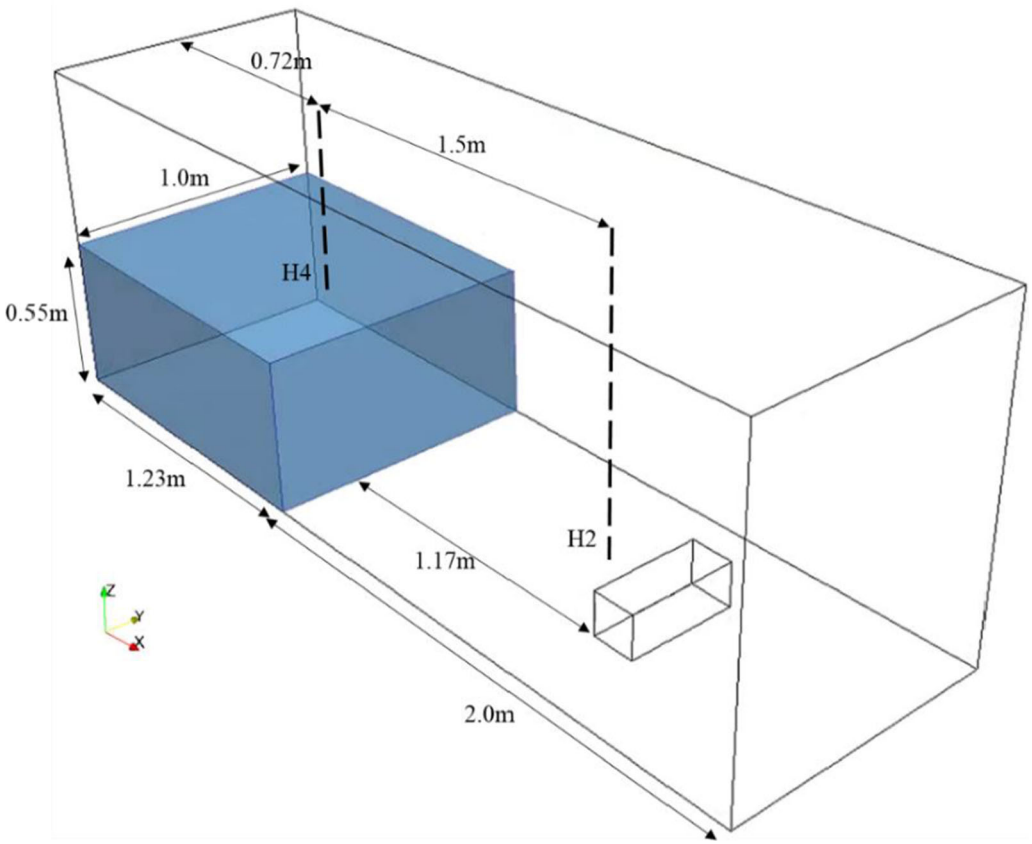

Fig. 8 Complex dambreak model used in this study

3.2 Dambreak test II

To further emphasize the validity of the parameters suggested in Sect. 3.1 ($\alpha = 0.01, \delta = 0.1$ and h = 1.2dp) and the accuracy of the SPH algorithm, a more complex dambreak by Kleefsman [23] is used. As shown in Fig. 8, a box of 0.161 m × 0.403 m × 0.161 m is fixed in the tank of 3.22 m × 1 m × 1 m, with a water column of 0.55 m height in the left. During the simulation, the water depth at point H2, H4 are recorded and used for the comparisons with the laboratory test. Furthermore, the effects of particle resolution are examined by 3 numerical tests P1-P3 with particle resolution dp = 1.83 cm, 1.0 cm, 0.8 cm, respectively.

Figure 9 shows the flow field of the complex dambreak test by experiment and numerical tests at different times, respectively. Figure 10 shows the evolution of water surface at monitoring points H2 and H4 from experimental and numerical tests. It can be seen that the results obtained by numerical tests match well with that of the laboratory test. When the door opened, the height of H4 gradually decreases which correspond well with the experiment (Fig. 10). After the flood collided with the box, the water bypass the box and formed a high water level at the right side and above the box (Fig. 9, 1.5 *s*). Then, the backflow reaches H2 and remains the peak value until 2.3 s before the water elevation begins to decrease (Fig. 10a). The backflow passes H4 at about 3 s and hit the tank again at the left boundary and the returning wave caused a new high water surface elevation at about 3.8 s at H4 (Fig. 9, 3.5 s, Fig. 10b).

From Fig. 9, although the flow fields of the four tests are approximately the same as the experiment, the fluid distribution of $P1$ around the box is not well enough when the fluid collided with the box at 0.75 s and 1.5 s compared with the other two tests ($P2$, $P3$). As the particle resolution increases, the flow field simulated is more refined, and a more obvious splashing phenomenon can be found as the water collides with the solid boundary. Furthermore, from Fig. 10, it can also be seen that the evolution of the water elevation of $P1$ from 0.5 s to 1.5 s are greatly different from other cases and experimental results as it fluctuates up and down, which indicates the particle elevation is not enough. As the newly formed backflow passes H2 from

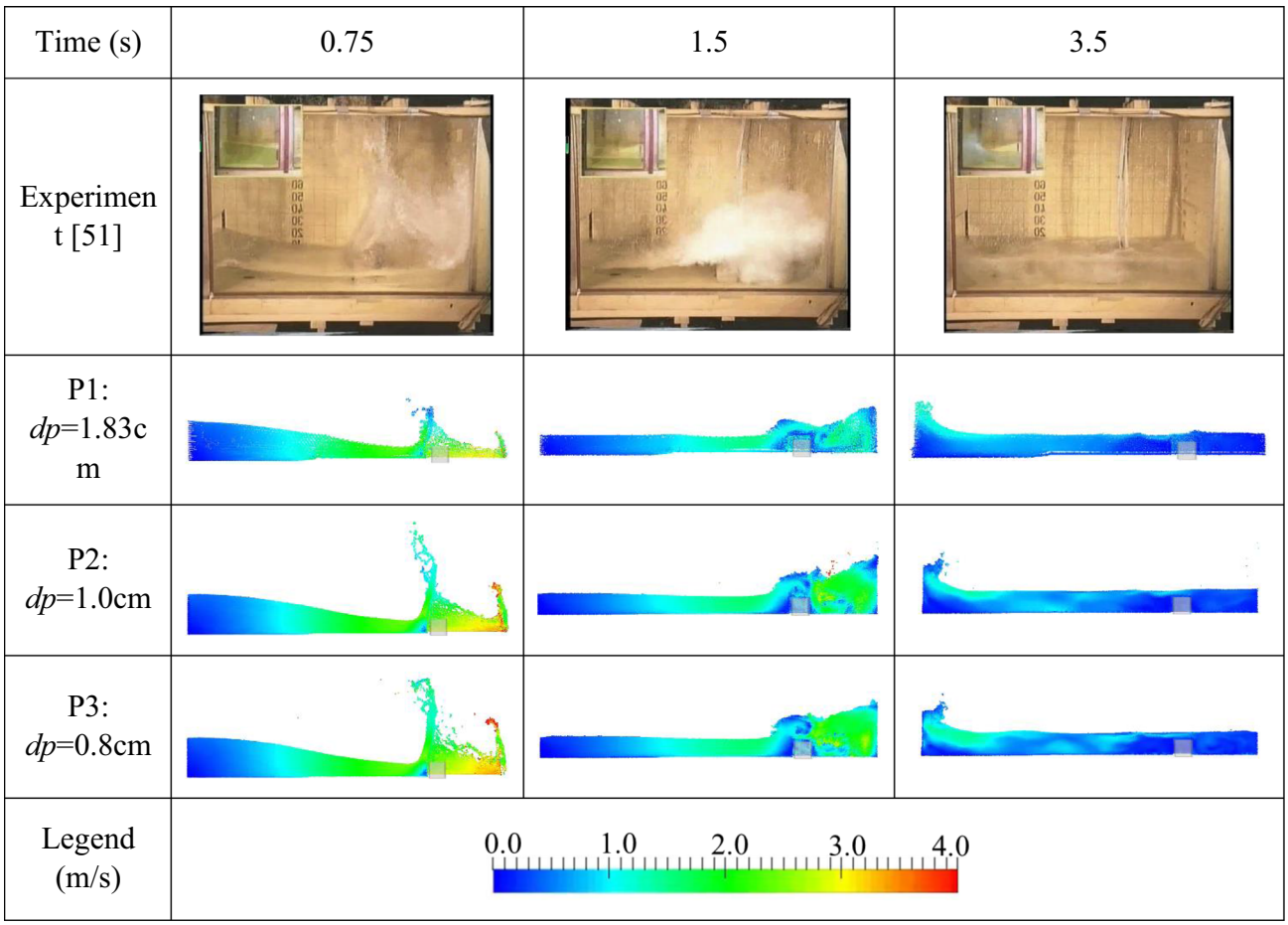

Fig. 9 Flow field of complex dambreak model by experiment and numerical results at different times

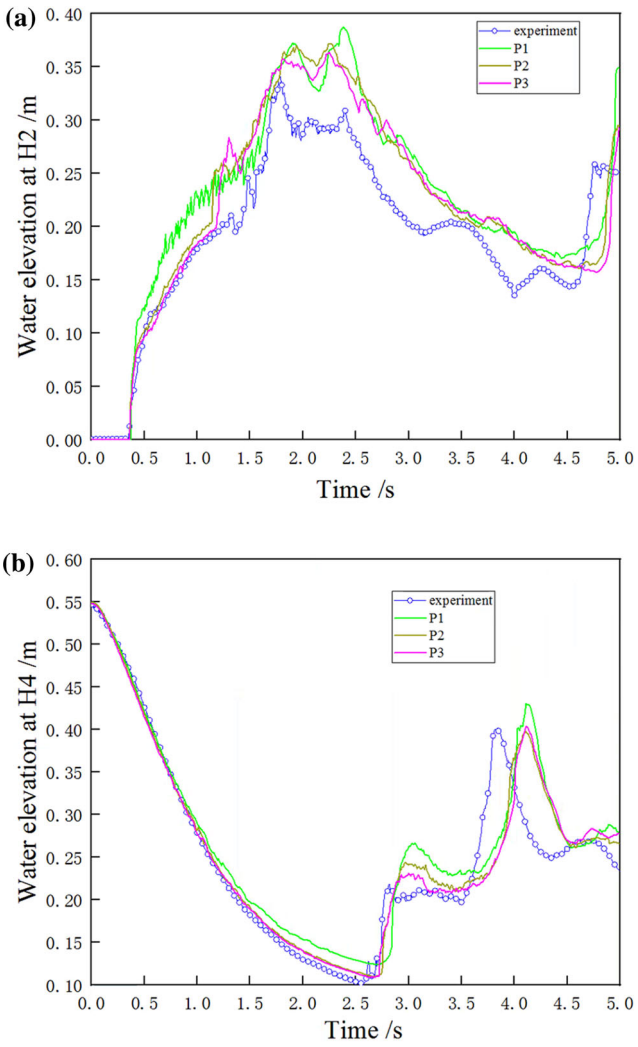

Fig. 10 The evolution of the water elevation at monitoring points by different particle resolution **a** H2 **b** H4

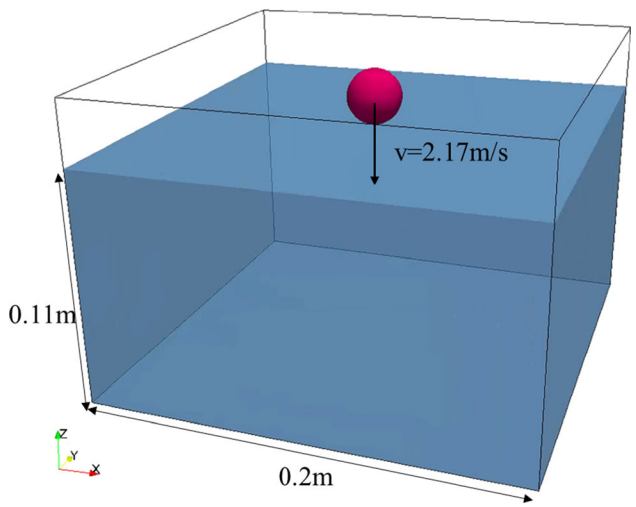

Fig. 11 Water entry test of a single sphere

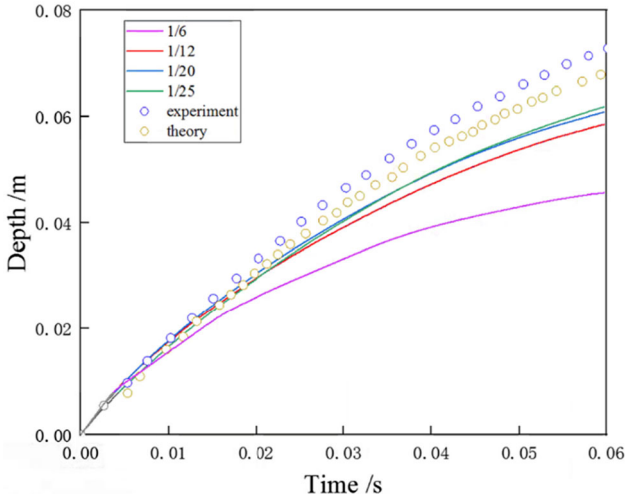

Fig. 12 Evolution of sphere's water entry depth with time

1.3 s to 2.5 s, the water elevations by *P*2, *P*3 are higher than the experiment due to some splashed water particles. The water elevation at H2 by numerical tests is similar to the experiment in terms of trend despite some high value during the decrease process from 2.5 s to 3.5. Comparing the water elevation at H4, it can be seen that the curves by *P*2, *P*3 are more acceptable than *P*1. Although there is a slight phase difference at 3.8 s after the backflow hit the left boundary of the tank, the water surface by *P*2, *P*3 matches well the experiment.

In an SPH model, the particle resolution should be compatible with the characteristic length (*lc*) to better simulate the flow field, wave, etc. while a precise model may largely decrease computation efficiency. In this model, the water depth can be regarded as characteristic length because the number of particles in depth direction should be sufficient to simulate the wave during the dam-break process. Taking the final water elevation 0.25 m as the characteristic length, the particle resolution dp = *0.01 m* is suggested, thereby 1/25*lc* is a proper particle interval in the SPH model.

As a whole, for a better simulation of the fluid dynamics by using SPH, the following conditions may be suggested and are used in the following simulations of this study and the companion study:

(1) a suitable diffusion term $\alpha = 0.01, \delta = 0.1$ is used.
(2) the smoothing length should be at about 1.2dp.
(3) the particle's resolution dp should be smaller than 1/25 times of characteristic length *lc*.

4 Validation of SPH–DEM coupling algorithm

DEM has proven efficient to simulate the solid phase and SPH can accurately simulate the fluid phase as shown in the previous benchmarks. The following benchmarks are used to validate the accuracy of the fluid–solid interactions.

For the coupling process between SPH and DEM, the ratio of the SPH particle's resolution (dp) to the DEM particle's diameter (D) will greatly influence the accuracy of the coupling algorithm. In this section, two cases are used: one is the water entry test of a single sphere, which is used to verify the SPH–DEM coupling algorithm, and taking as the example for the study of the influence of dp/D on the coupling process of the looser spheres assembly (not contact each other) with the fluid; the other is the tsunami process of a slide, for the study of the influence of dp/D on the coupling process of the closely contacted spheres

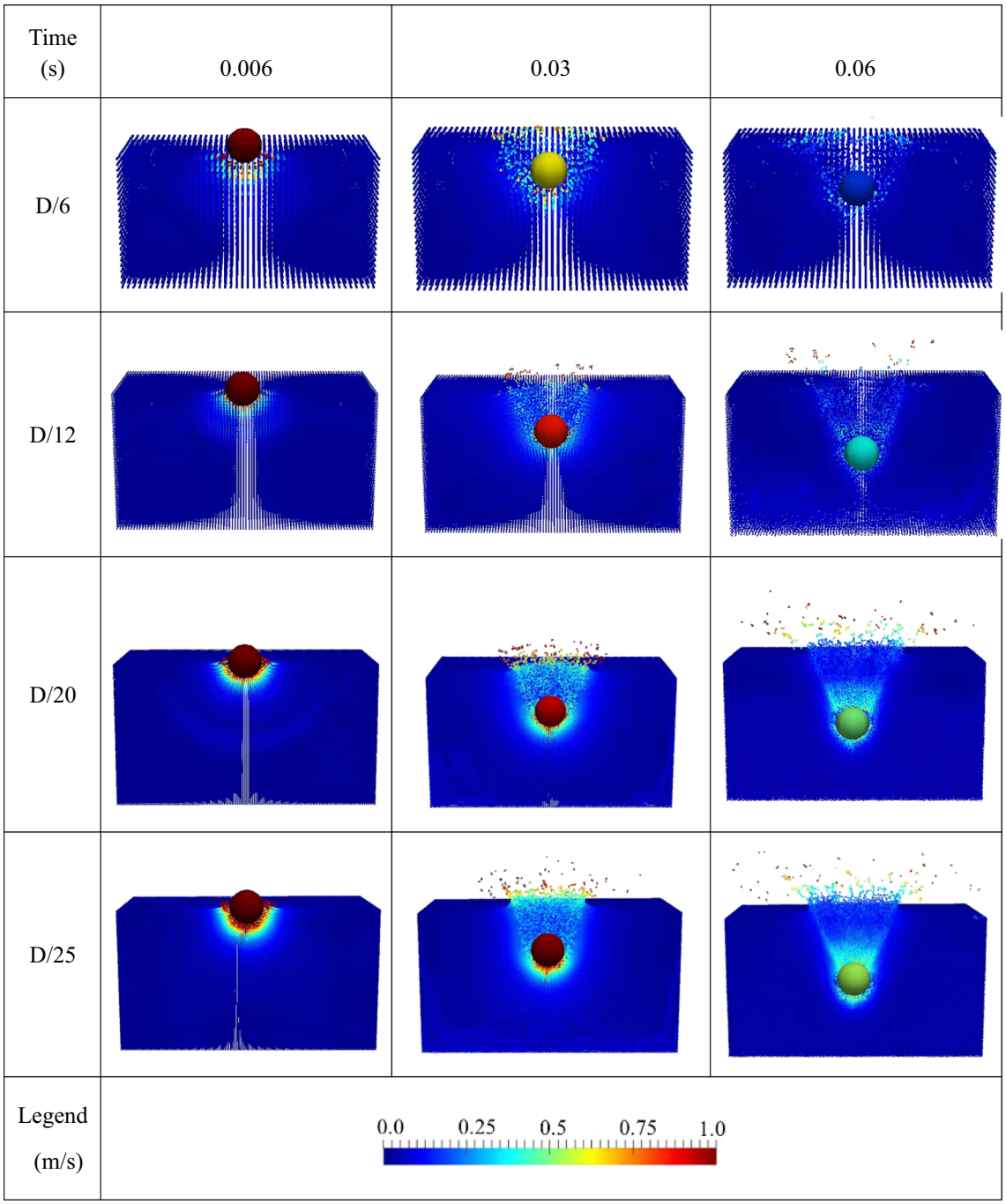

Fig. 13 Flow field by different particle resolution at different time

assembly with the fluid. The parameters suggested in Sect. 3.2 are used in SPH.

4.1 Water entry test of a single sphere

A water entry test of a single sphere by Aristoff [4] is used to verify the SPH–DEM coupling algorithm for the interaction between the fluid (SPH) and solid particle (DEM). As illustrated in Fig. 11, a tank of 0.2 m × 0.2 m × 0.14 m is filled with water of 0.11 m in depth. A sphere of radius 12.7 mm is released under gravity (9.8 m/s^2) in tangency with the water surface at an initial speed of 2.17 m/s in verticle direction. The density of the sphere and water is 860 kg/m^3 and 1000 kg/m^3, respectively. To study the influence of SPH particles' resolution on the numerical result, four parallel tests are performed with different sizes of dp for SPH particles: D/6, D/12, D/20, D/25 (where D is the sphere's diameter). The error between numerical results and theoretical results are monitored and compared [8, 41].

Figure 12 shows the evolution of water entry depth with time obtained by the numerical tests and the experiment. Figure 13 shows the flow field of the four cases at different times. As illustrated in Fig. 12, with the increase of SPH particle resolution, the depth simulated is closer to the experimental and theoretical results. As depicted in Fig. 13, at the initial stage, the sphere presses the water and the particles on the side of the sphere moves upwards and sidewards (Fig. 13, *0.006 s*). The sphere then drops into the water at a relatively high speed, leaving a cavity above it (Fig. 13, *0.03 s*). At 0.06 s, due to the water pressure around, the cavity is about to collapse (Fig. 13, *0.06 s*). However, for lower SPH resolution, such as dp = D/6, the size of the cavity is larger due to the "gap effect" which is discussed in Sect. 3.1 , thereby the solid particles pushed more water aside which increases the buoyancy and the energy consumption. With the increase of SPH resolution, the "gap effect" is decreased and the numerical results are closer to the physical test. Comparing the final results, the error of depth obtained by dp = D/6 from theoretical result is about 33%. The error decreases to 14%, 10%, 10% as the SPH particle interval reduces to D/12, D/20, respectively.

Furthermore, as the dp < D/20, there are few influences on the numerical results. So, for the DEM with a single sphere or looser spheres assembly (not contact each other), to ensure the accuracy of the interaction forces between solid particle and fluid based on the coupled SPH–DEM algorithm, the SPH particle resolution dp should be smaller than 1/20 the diameter of DEM particle.

4.2 Tsunami process of a slide

Generally, the granular particles in DEM are tightly contacted, and in some cases (such as landslide tsunami, dam breach, and so on) the fluid domain is greatly larger than the particle size. If the dp < D/20 is used, which will make the number of SPH particles too large to take a long time for simulation, or exceed the current computing power of the computer.

Table 2 Mechanical parameters of DEM models in landslide tests

Parameters	Sphere	Boundary
Density (kg/m^3)	2500	–
Young's module (MPa)	1.0	5.0
Poisson ratio	0.2	0.2
Friction angle (°)	30.0	10.0
Normal cohesion (kPa)	0	0
Shear cohesion (kPa)	0	0

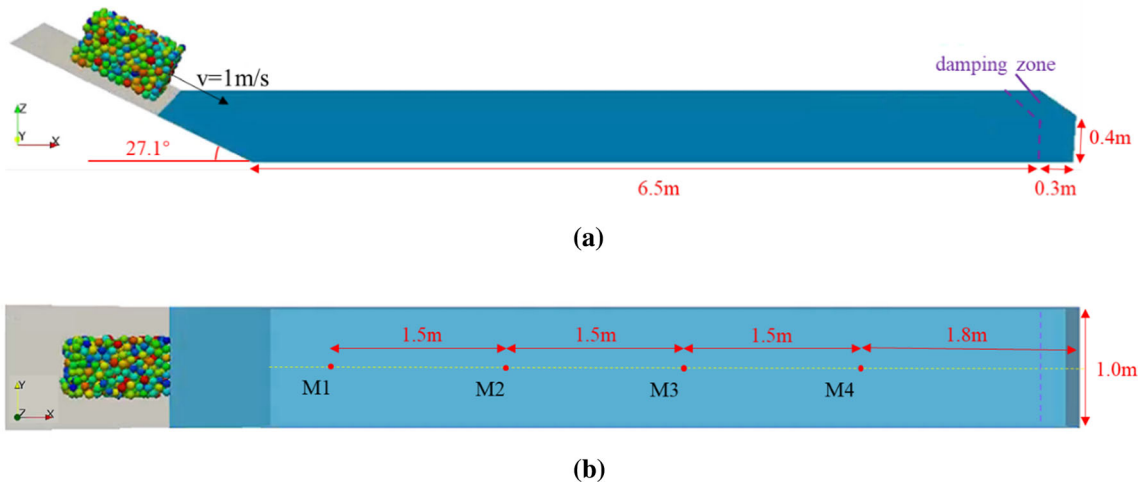

Fig. 14 Tsunami test of a slide composed by a series of spherical particles: **a** side view; **b** top view

Considering that the errors due to resolution (dp/D) are mainly caused by the gap between the sphere and water, the gap effects may be decrease for the solid particles with tightly contacted. Because in this case, the volume of the gap is negligible compared with the volume of the total granular assembly. In this section, the tsunami process of a slide composed of a series of spherical particles is used to study the influence of dp/D on the coupling simulation between the granular particles that are tightly in contact with the fluid.. As shown in Fig. 14a tank with a bottom surface of 6.8 m × 1.0 m is filled with water of 0.4 m in depth. At the side of the container is a slope of 27.1 ° with a slide body composed of 522 spheres that has radii of 0.03 m, which are sliding down at an initial velocity of 1 m/s. Four numerical tests are performed with different values of dp/D = 1/4, 1/6, 1/8, and 1/10, respectively. The mechanical parameters of the simulation are shown in Table 2. During the simulation, for the comparisons of different tests, the water surface elevations at four monitoring points M1, M2, M3, and M4 are recorded (Fig. 14).

Figure 15 shows the displacement of the slide body for four tests, and Fig. 16 shows the interaction between the SPH particles and DEM particles near the water entry position at 3 s. As shown in Fig. 15, the value of the dp/D will influence the shape of the deposit: for the test with smaller dp/D, the displacement of the front part of the slide will be larger (Fig. 15c and d).

During the water entry process, the solid DEM particles will interact with the fluid SPH particles and push them away, thereby generating the tsunami. In a coarse model such as dp = D/4, the size of the support region is large and the pressure field (Eqs. 18, 20) of solid particles inside the support region prevents the SPH fluid particles from entering the pores among the DEM spheres (Fig. 16a). In

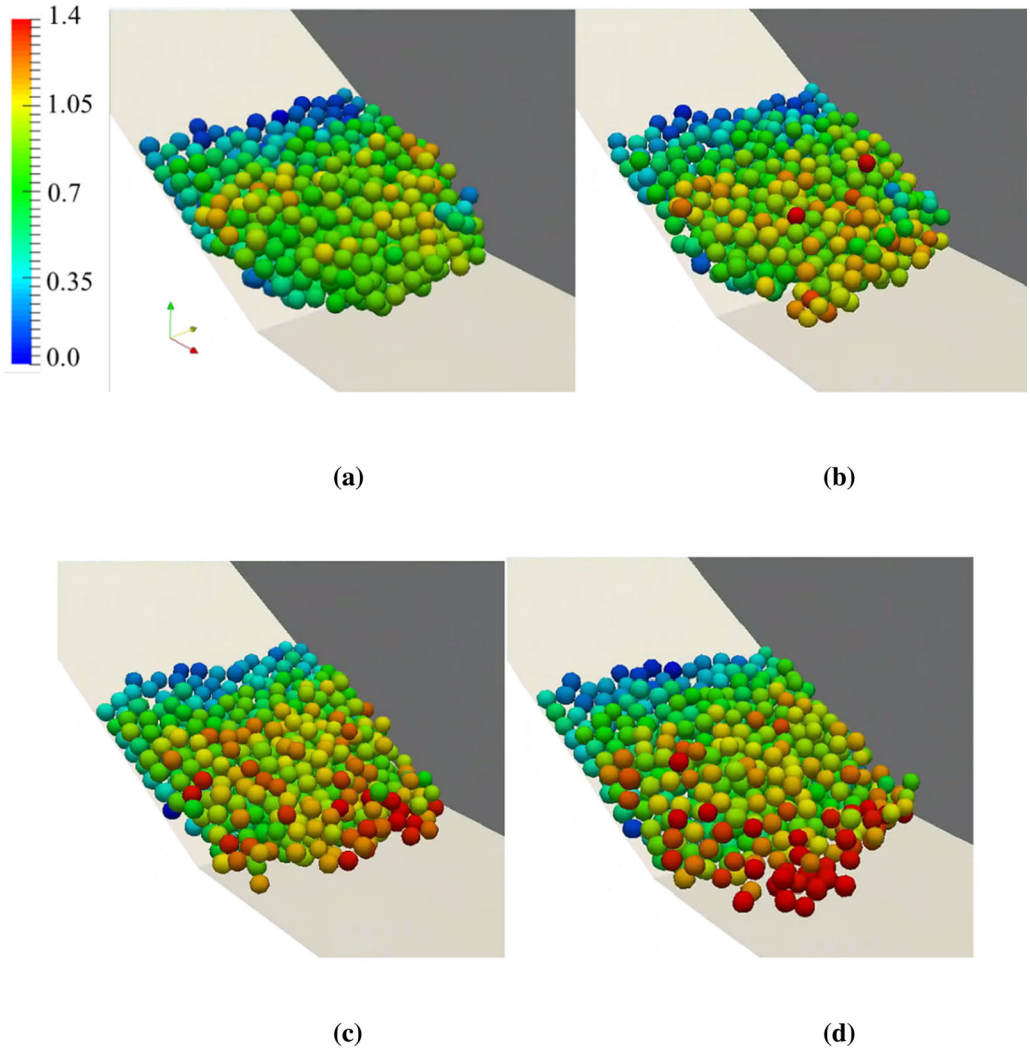

Fig. 15 Displacement (m) of the slide by the four tests with different dp: **a** dp = D/4; **b** dp = D/6; **c** dp = D/8; **d** dp = D/10

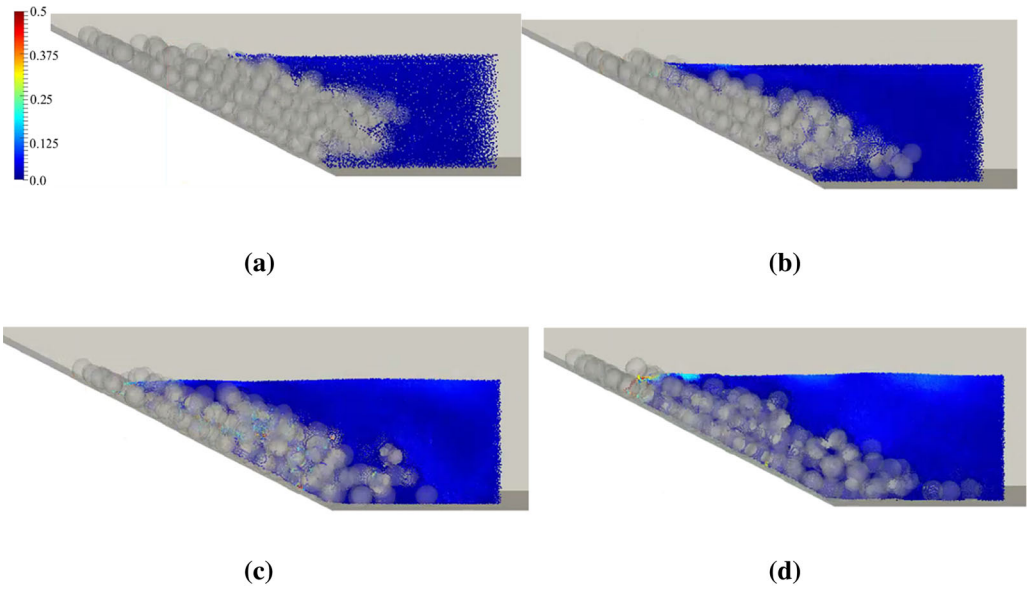

Fig. 16 The interaction between the SPH particles and DEM particles near the water entry position by the four tests with different dp (time = 3 s): **a** dp = D/4; **b** dp = D/6; **c** dp = D/8; **d** dp = D/10

this case, the fluid pressure around the deposit will tightly press the spheres together (Fig. 16a). Conversely, in a fine model like dp = D/10, the fluid SPH particles can enter the pores among the DEM spheres (Fig. 16d) thereby balancing the pressure around the spheres, so the spheres at the front scattered around. Comparing the slide displacement (Fig. 15) and the interaction between SPH particles and DEM particles (Fig. 16), dp $\leq$ D/8 will be better to obtain a feasible simulation of the depositing process of the slide.

Figures 17 and 18 show the water surface elevation of the four monitoring points and the water surface at different times by the four tests, respectively. From Fig. 17, the water elevations at M1 from 0.4 to 1.0 s do not match very well with each other due to some splashes as the granular material is accelerated into the water. While for M2, M3 and M4, the water elevations of the four tests are approximately identical. According to the evolution of the water surface at different times (Fig. 18), except near the water entry position, it can be seen that the water surface of the four tests matches well with each other.

During the simulation, the kinetic energy of the granular material is transferred to the water, and the tsunami is generated. The value of the dp/D will influence the interaction between the SPH particles and DEM particles on meso-scale, and then influence the fluid field near the water entry position of the slide. While, the total kinetic energy of the slide and the volume of slide entry the water are similar for the four tests with different dp, so the tsunamis are also similar, especially in the far field (beyond M2).

So, considering the depositing and tsunami process of the slide, the value of the dp should not greater than D/6 or D/8 for a more refined simulation. According to the simulation requirements, it is possible to appropriately decrease the particle resolution to save the computation cost while remain high accuracy in large-scale simulation of landslide-induced tsunami.

5 Conclusion

Landslide triggered tsunami is an important subject in the study of the disaster chain. The algorithm for the fluid phase, solid phase and fluid–solid interaction process is crucial but also a challenge in the simulation of landslide-induced waves. Fortunately, the development of SPH, DEM and SPH–DEM coupling methods provides a way to analyze the disaster process. In this study, the SPH–DEM

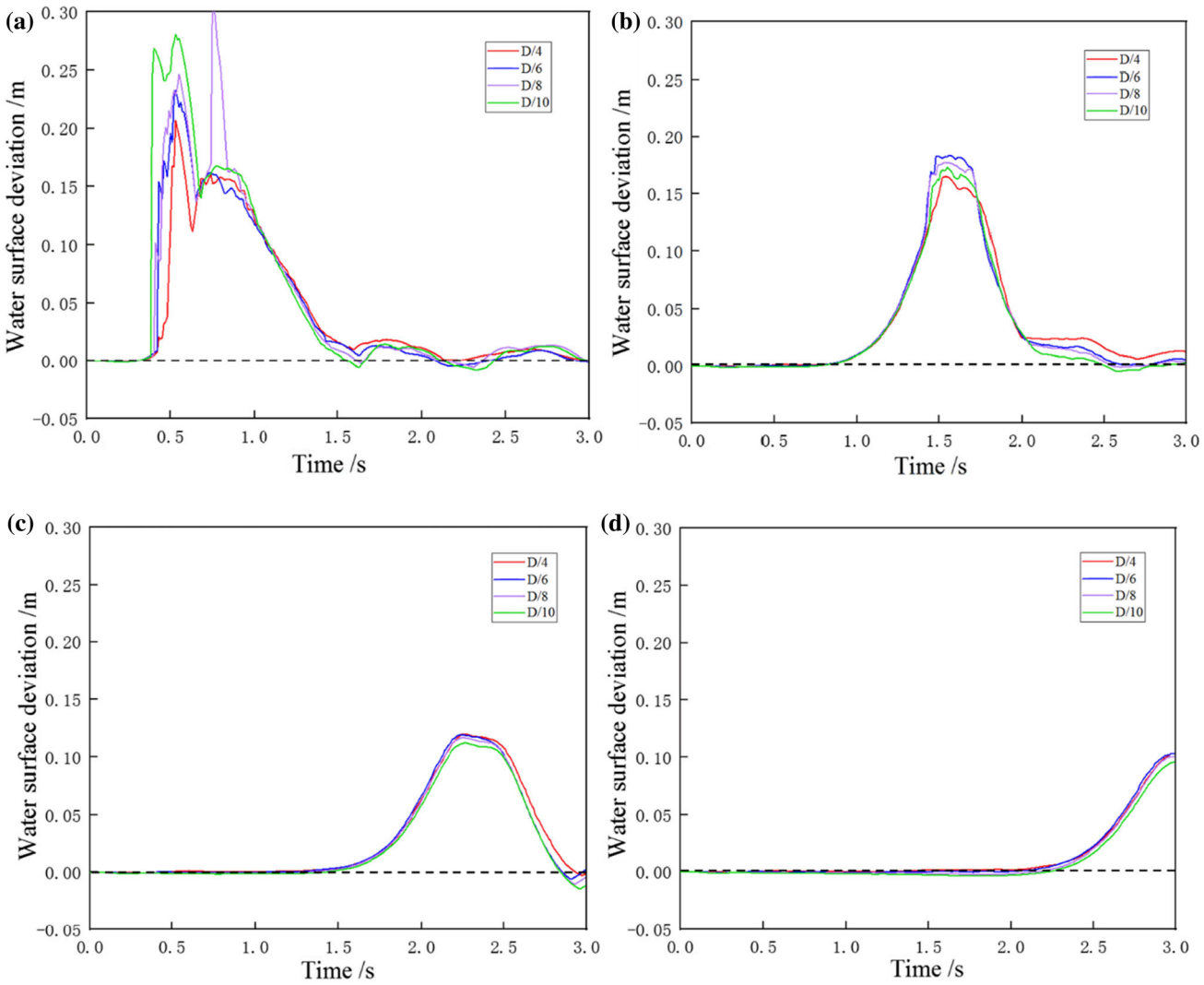

Fig. 17 Evolution of water surface deviation at the four monitoring points with time: **a** M1; **b** M2; **c** M3; **d** M4

coupling code CoSim based on multi-GPU is developed and validated for the practical case in the companion paper.

Based on two dambreak tests, the influence of diffusion term, smoothing length, and particle interval on the flow field simulation of SPH are studied, respectively. Considering both the accuracy and efficiency in SPH simulation, some parameters are suggested: the diffusion term $\alpha = 0.01, \delta = 0.1$; h = 1.2 dp; and dp should be smaller than 1/25 times that of the characteristic length of the model.

The water entry test of a single sphere and the tsunami process of a slide are used to verify the accuracy of the SPH–DEM coupling algorithm under different conditions. The ratio of the SPH particle's resolution (dp) to the DEM particle's diameter (D) will greatly influence the accuracy of the SPH–DEM coupling simulation. To ensure the accuracy of the interaction between solid and fluid based on the coupled SPH–DEM algorithm, when DEM mode is a single sphere or the looser spheres assembly (not contact each other), dp/D $\leq$ 1/20 is suggested; while when the granular particles in DEM are tightly in contact, the dp/D $\leq$ 1/6 or $\leq$ D/8 for more refined simulation will be enough.

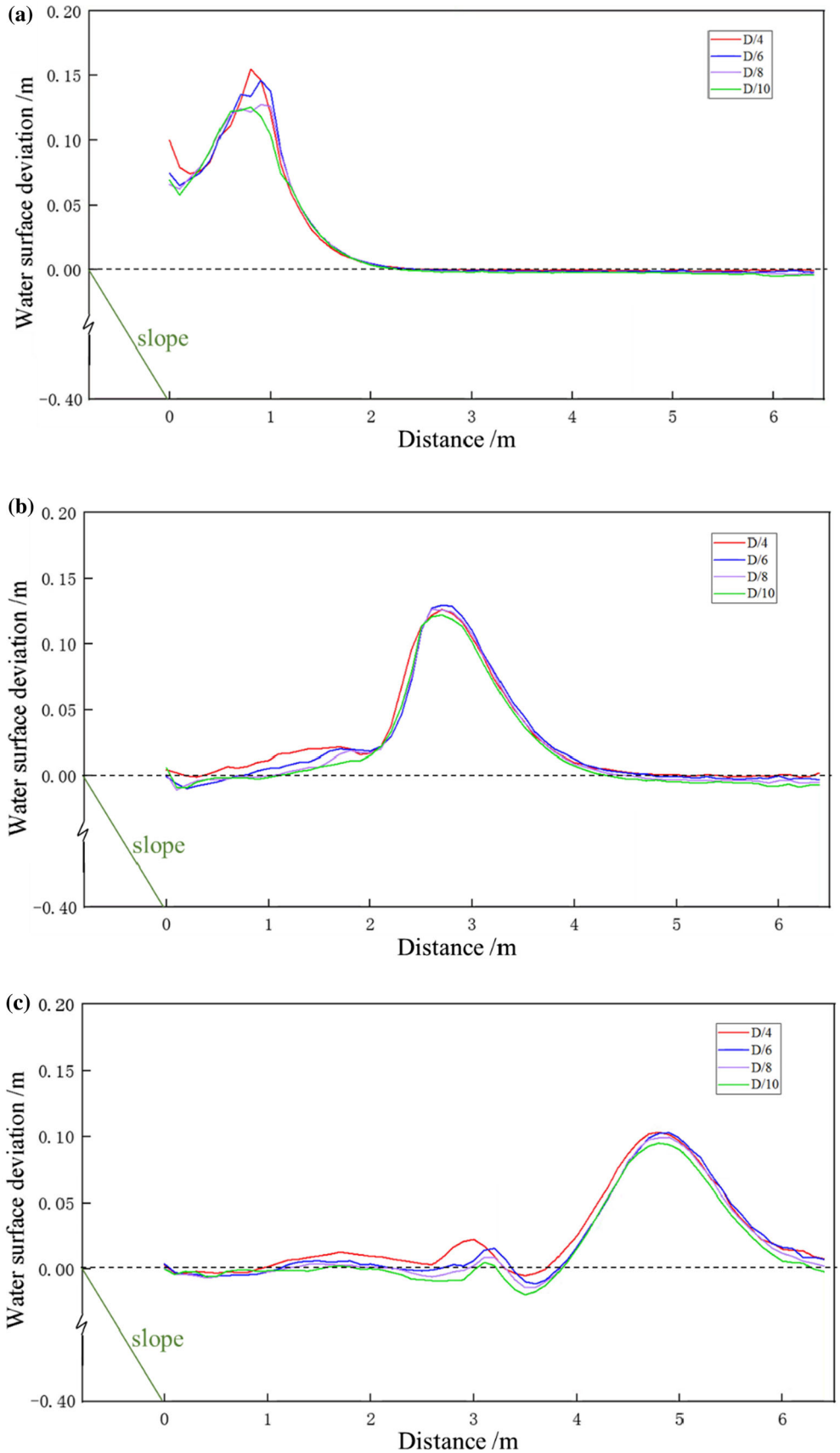

Fig. 18 Water surface deviation at different time: **a** 1 s; **b** 2 s; **c** 3 s

Acknowledgements The authors would like to acknowledge the project of "Natural Science Foundation of China, China (51879142, 52079067)" and "Research Fund Program of the State Key Laboratory of Hydroscience and Engineering (2020-KY-04)."

Data availability No data, models, or code were generated or used during the study.

Declarations

Conflict of interest The authors declared that they have no conflicts of interest to this work.

References

1. Adami S, Hu XY, Adams NA (2012) A generalized wall boundary condition for smoothed particle hydrodynamics. J Comput Phys 231:7057–7075. https://doi.org/10.1016/j.jcp.2012.05.005
2. Anderson JA, Lorenz CD, Travesset A (2008) General purpose molecular dynamics simulations fully implemented on graphics processing units. J Comput Phys 227:5342–5359. https://doi.org/10.1016/j.jcp.2008.01.047
3. Antuono M, Colagrossi A, Marrone S (2012) Numerical diffusive terms in weakly-compressible SPH schemes. Comput Phys Commun 183:2570–2580. https://doi.org/10.1016/j.cpc.2012.07.006
4. Aristoff JM, Truscott TT, Techet AH, Bush JWM (2010) The water entry of decelerating spheres. Phys Fluids 22:1–8. https://doi.org/10.1063/1.3309454
5. Bosa S, Petti M (2013) A numerical model of the wave that overtopped the Vajont Dam in 1963. Water Resour Manag 27:1763–1779. https://doi.org/10.1007/s11269-012-0162-6
6. Burman BC, Cundall PA, Strack ODL (1980) A discrete numerical model for granular assemblies. Geotechnique 30:331–336. https://doi.org/10.1680/geot.1980.30.3.331
7. Canelas RB, Crespo AJC, Domínguez JM et al (2016) SPH-DCDEM model for arbitrary geometries in free surface solid-fluid flows. Comput Phys Commun 202:131–140. https://doi.org/10.1016/j.cpc.2016.01.006
8. Cheng H, Luding S, Rivas N, Harting J, Magnanimo V (2019) Hydro-micromechanical modeling of wave propagation in saturated granular crystals. Int J Numer Anal Methods Geomech 43:1115–1139. https://doi.org/10.1002/nag.2920
9. Crespo AJC, Domínguez JM, Rogers BD et al (2015) DualSPHysics: open-source parallel CFD solver based on smoothed particle hydrodynamics (SPH). Comput Phys Commun 187:204–216. https://doi.org/10.1016/j.cpc.2014.10.004
10. Crosta GB, Imposimato S, Roddeman D (2016) Landslide spreading, impulse water waves and modelling of the Vajont rockslide. Rock Mech Rock Eng 49:2413–2436. https://doi.org/10.1007/s00603-015-0769-z
11. Ding WT, Xu WJ (2018) Study on the multiphase fluid-solid interaction in granular materials based on an LBM-DEM coupled method. Powder Technol 335:301–314. https://doi.org/10.1016/j.powtec.2018.05.006
12. Eliáš J (2014) Simulation of railway ballast using crushable polyhedral particles. Powder Technol 264:458–465. https://doi.org/10.1016/j.powtec.2014.05.052
13. Fritz H, Hager W, Minor H-E (2001) Lituya Bay case: rockslide impact and wave run-up. Sci Tsunami Hazards 19:3–19
14. Fujisawa K, Murakami A, Nishimura S, Shuku T (2012) Relation between seepage force and velocity of sand particles during sand boiling. Geotech Eng 44:9–17
15. Gingold RA, Monaghan JJ (1977) Smoothed particle hydrodynamics: theory and application to non-spherical stars. Mon Not R Astron Soc 181:375–389. https://doi.org/10.1093/mnras/181.3.375
16. Govender N, Rajamani RK, Kok S, Wilke DN (2015) Discrete element simulation of mill charge in 3D using the BLAZE-DEM GPU framework. Miner Eng 79:152–168. https://doi.org/10.1016/j.mineng.2015.05.010
17. Govender N, Wilke DN, Kok S (2015) Blaze-DEMGPU: modular high performance DEM framework for the GPU architecture. SoftwareX 5:62–66. https://doi.org/10.1016/j.softx.2016.04.004
18. Guo N, Zhao J (2016) 3D multiscale modeling of strain localization in granular media. Comput Geotech 80:360–372. https://doi.org/10.1016/j.compgeo.2016.01.020
19. He Y, Bayly AE, Hassanpour A et al (2018) A GPU-based coupled SPH-DEM method for particle-fluid flow with free surfaces. Powder Technol 338:548–562. https://doi.org/10.1016/j.powtec.2018.07.043
20. Hérault A, Bilotta G, Dalrymple RA (2010) SPH on GPU with CUDA. J Hydraul Res 48:74–79. https://doi.org/10.1080/00221686.2010.9641247
21. Iverson RM (1997) The physics of debris flow. Rev Geophys 35:245–296
22. Kermani E, Qiu T (2020) Simulation of quasi-static axisymmetric collapse of granular columns using smoothed particle hydrodynamics and discrete element methods. Acta Geotech 15:423–437. https://doi.org/10.1007/s11440-018-0707-9
23. Kleefsman KMT, Fekken G, Veldman AEP et al (2005) A volume-of-fluid based simulation method for wave impact problems. J Comput Phys 206:363–393. https://doi.org/10.1016/j.jcp.2004.12.007
24. Kloss C, Goniva C, Hager A et al (2012) Models, algorithms and validation for opensource DEM and CFD-DEM. Prog Comput Fluid Dyn 12:140–152. https://doi.org/10.1504/PCFD.2012.047457
25. Koshizuka S, Oka Y, Tamako HA (1995) A particle method for calculating splashing of incompressible viscous fluid. Proc. International Conf. Mathematics and Computations, Reactor Physics and Environmental Analyses, Portland, 1514-1521. CONF-950420-TRN: 97:001160-0134
26. Lee E-S, Violeau D, Issa R, Ploix S (2010) Application of weakly compressible and truly incompressible SPH to 3-D water collapse in waterworks. J Hydraul Res 48:50–60. https://doi.org/10.1080/00221686.2010.9641245
27. Li T, Wu A, Feng Y et al (2018) Coupled DEM-LBM simulation of saturated flow velocity characteristics in column leaching. Miner Eng 128:36–44. https://doi.org/10.1016/j.mineng.2018.08.027
28. Li X, Zhao J (2018) Dam-break of mixtures consisting of non-Newtonian liquids and granular particles. Powder Technol 338:493–505. https://doi.org/10.1016/j.powtec.2018.07.021
29. Liao H, Wang Y, Li Y et al (2020) 3D fluid-solid coupling simulation for plate-type nuclear fuel assemblies under the irradiation condition. Prog Nucl Energy 126:103428. https://doi.org/10.1016/j.pnucene.2020.103428
30. Liu GY, Xu WJ, Govender N, Wilke DN (2020) A cohesive fracture model for discrete element method based on polyhedral blocks. Powder Technol 359:190–204. https://doi.org/10.1016/j.powtec.2019.09.068
31. Locat J, Lee HJ (2002) Submarine landslides: advances and challenges. Can Geotech J 39:193–212. https://doi.org/10.1139/t01-089

32. Lubbe R, Xu WJ, Wilke DN et al (2020) Analysis of parallel spatial partitioning algorithms for GPU based DEM. Comput Geotech 125:103708. https://doi.org/10.1016/j.compgeo.2020.103708
33. Marrone S, Antuono M, Colagrossi A et al (2011) δ-SPH model for simulating violent impact flows. Comput Methods Appl Mech Eng 200:1526–1542. https://doi.org/10.1016/j.cma.2010.12.016
34. Masson DG, Harbitz CB, Wynn RB et al (2006) Submarine landslides: Processes, triggers and hazard prediction. Philos Trans R Soc A Math Phys Eng Sci 364:2009–2039. https://doi.org/10.1098/rsta.2006.1810
35. Molteni D, Colagrossi A (2009) A simple procedure to improve the pressure evaluation in hydrodynamic context using the SPH. Comput Phys Commun 180:861–872. https://doi.org/10.1016/j.cpc.2008.12.004
36. Monaghan JJ (1992) Smoothed particle hydrodynamics. Annu Rev Astron Astrophys 30:543–574. https://doi.org/10.1146/annurev.aa.30.090192.002551
37. Monaghan JJ (1994) Simulating free surface flows with SPH. J Comput Phys 110:399–406. https://doi.org/10.1006/jcph.1994.1034
38. Natsui S, Sawada A, Terui K et al (2018) DEM-SPH study of molten slag trickle flow in coke bed. Chem Eng Sci 175:25–39. https://doi.org/10.1016/j.ces.2017.09.031
39. Peng C, Zhan L, Wu W, Zhang B (2021) A fully resolved SPH-DEM method for heterogeneous suspensions with arbitrary particle shape. Powder Technology, Elsevier B.V vol 387(April): pp 509–526.
40. Ren B, Jin Z, Gao R et al (2014) SPH-DEM modeling of the hydraulic stability of 2D blocks on a slope. J Waterw Port Coast Ocean Eng 140:04014022. https://doi.org/10.1061/(asce)ww.1943-5460.0000247
41. Robinson M, Ramaioli M, Luding S (2014) Fluid-particle flow simulations using two-way-coupled mesoscale SPH-DEM and validation. Int J Multiph Flow 59:121–134. https://doi.org/10.1016/j.ijmultiphaseflow.2013.11.003
42. Saadlaoui Y, Delache A, Feulvarch E et al (2020) New strategy of solid/fluid coupling during numerical simulation of thermo-mechanical processes. J Fluids Struct 99:103161. https://doi.org/10.1016/j.jfluidstructs.2020.103161
43. Sarfaraz M, Pak A (2017) An integrated SPH-polyhedral DEM algorithm to investigate hydraulic stability of rock and concrete blocks: application to cubic armours in breakwaters. Eng Anal Bound Elem 84:1–18. https://doi.org/10.1016/j.enganabound.2017.08.002
44. Shen J, Wheeler C, Ilic D, Chen J (2019) Application of open source FEM and DEM simulations for dynamic belt deflection modelling. Powder Technol 357:171–185. https://doi.org/10.1016/j.powtec.2019.08.068
45. Sinnott MD, Cleary PW, Morrison RD (2017) Combined DEM and SPH simulation of overflow ball mill discharge and trommel flow. Miner Eng 108:93–108. https://doi.org/10.1016/j.mineng.2017.01.016
46. Tabib MV, Roy SA, Joshi JB (2008) CFD simulation of bubble column—An analysis of interphase forces and turbulence models. Chem Eng J 139:589–614. https://doi.org/10.1016/j.cej.2007.09.015
47. Tan H, Chen S (2017) A hybrid DEM-SPH model for deformable landslide and its generated surge waves. Adv Water Resour 108:256–276. https://doi.org/10.1016/j.advwatres.2017.07.023
48. Wang J, Wang S, Su A, Xiang W, Xiong CR, Blum P (2021) Simulating landslide-induced tsunamis in the Yangtze River at the three gorges in China. Acta Geotech 16:2487–2503
49. Wendland H (1995) Piecewise polynomial, positive definite and compactly supported radial functions of minimal degree. Adv Comput Math 4:389–396. https://doi.org/10.1007/BF02123482
50. Wu K, Yang D, Wright N (2016) A coupled SPH-DEM model for fluid-structure interaction problems with free-surface flow and structural failure. Comput Struct 177:141–161. https://doi.org/10.1016/j.compstruc.2016.08.012
51. Xu WJ, Dong XY (2021) Simulation and verification of landslide tsunamis using a 3D SPH-DEM coupling method. Comput Geotech 129:103803. https://doi.org/10.1016/j.compgeo.2020.103803
52. Xu WJ, Dong XY, Ding WT (2019) Analysis of fluid-particle interaction in granular materials using coupled SPH-DEM method. Powder Technol 353:459–472. https://doi.org/10.1016/j.powtec.2019.05.052
53. Xu WJ, Yao ZG, Luo YT, Dong XY (2020) Study on landslide-induced wave disasters using a 3D coupled SPH-DEM method. Bull Eng Geol Environ 79:467–483. https://doi.org/10.1007/s10064-019-01558-3
54. Zhan L, Peng C, Zhang B, Wu W (2019) A stabilized TL–WC SPH approach with GPU acceleration for three-dimensional fluid–structure interaction. J. Fluids Struct, Elsevier Inc. vol 86: pp 329–353
55. Zhan L, Peng C, Zhang B, Wu W (2021) A surface mesh represented discrete element method (SMR-DEM) for particles of arbitrary shape. Powder Technol, Elsevier B.V. vol 377: pp 760–779
56. Zhang S, Yin Y, Hu X et al (2020) Dynamics and emplacement mechanisms of the successive baige landslides on the upper reaches of the Jinsha River China. Eng Geol 278:105819. https://doi.org/10.1016/j.enggeo.2020.105819
57. Zheng Z, Zang M, Chen S, Zeng H (2018) A GPU-based DEM-FEM computational framework for tire-sand interaction simulations. Comput Struct 209:74–92. https://doi.org/10.1016/j.compstruc.2018.08.011
58. Zhong W, Yu A, Liu X et al (2016) DEM/CFD-DEM modelling of non-spherical particulate systems: theoretical developments and applications. Powder Technol 302:108–152. https://doi.org/10.1016/j.powtec.2016.07.010
59. Zhou, Q., Xu, W., and Liu, G. (2021) Computers and geotechnics a contact detection algorithm for triangle boundary in GPU-based DEM and its application in a large-scale landslide. Comput Geotech, Elsevier Ltd vol 138(April): pp 104371.
60. Zhu C, Peng C, Wu, (2021) W. Applications of micropolar SPH in geomechanics. Acta Geotech 16:2355–2369. https://doi.org/10.1007/s11440-021-01177-x